INSIGHTS INTO PROVENANCE, TECTONIC CONTEXT, SEDIMENTARY AND DIAGENETIC PROCESSES FROM SÃO BENEDITO FORMATION ROCKS, AMAZON STATE, BRAZIL

João Gabriel Cavalcante Vieira[1]; Pamela Silveira Costa[1]; Adriana Maria Coimbra Horbe[1]; Dermeval Aparecido do Carmo[1].

1-Programa de Pós-graduação em Geologia, Instituto de Geociências, Universidade de Brasília, Campus Darcy Ribeiro, Asa Norte 70910-900, Brasília, DF, Brasil

ABSTRACT

The Alto Tapajós Basin remains unexplored and lacks published subsurface data. In the far northwestern basin region, the São Benedito Formation is known to contain shales, siltstones, and phosphate-bearing quartz-arenites. The phosphatic rocks add significance to the better understanding of the unit, given the vital role of this mineral resource in global agriculture and food production. In that context, the study aimed to contribute to fundamental aspects, such as depositional system, provenance, tectonic setting, sedimentary and diagenetic processes that influenced the São Benedito Formation rocks. The methodological approach included petrography, X-ray diffraction, electron microprobe analysis, whole-rock geochemistry, and Nd isotope analysis. The successions consist of sandstones, sandstones with mudstone interbeds, mudstones, dolomitic marls, dolostones, and rare breccias. The rocks present marine authigenic minerals, including fluorapatite, glauconite, siderite, pyrite, and dolomite. Deposition is interpreted to occur in a shallow marine environment dominated by storm activity, that transitioned from outer shelf to lower shoreface. Geochemistry data support intracratonic rift setting and some collisional signatures are believed to have been inherited from basement sedimentary rocks and their sources. Immobile trace elements and isotopic data reveal a mainly felsic upper continental crust source and probably no provenance changes linked to grain size variations. The presence of MREE enrichments on sandstones that yield anomalously high Nd model ages results from the presence of authigenic fluorapatite, enriched on MREE during diagenesis from the reduction of Fe oxyhydroxides and later from clay minerals desorption. MREE depletions on mudstones and an anomalously low Nd model age of 0.92 Ga for a mudstone sample corroborate the hypothesis. Nd isotopic data of mainly the fine-grained rocks represent the true weighted mean age of mantle extraction for the provenance components, which yielded T_{DM} = 2.29 – 2.57 Ga. Based on these results, the sources for the successions are related

to the local basement rocks from the Rondônia-Juruena Province. Tapajós-Parima Province's contribution isn't discarded as well. Exceptionally, one marl sample presented a much older T_{DM} age of 3.35 Ga, related to a possible contribution from Central Amazon Province rocks or unknown proximal units.

Keywords: Alto Tapajós Basin; Neodymium isotopes; Whole-rock geochemistry.

1 INTRODUCTION

Geochemical and isotopic techniques are potent tools for exploring the tectonic settings, provenance, and post-depositional processes that influenced siliciclastic sediments and sedimentary rocks (Dickinson & Suczek, 1979; Dickinson et al., 1983; Bhatia & Crook, 1986; McLennan et al., 1990, 1993; De Oliveira Carvalho et al., 2021; Paravidini et al., 2021). Typically, mudstones are preferred for geochemical and isotopic provenance studies due to their more uniformly mixed sources and lower susceptibility to alterations during deposition and diagenesis (Blatt, 1985; Cullers, 1995; Meinhold et al., 2022). However, studies that focus solely on muds and mudstones might lead to an overestimation of mafic contributions, and some successions might exhibit source differences dependent on grain size, thus it is required the evaluation of all particle sizes available on a succession (McLennan et al., 1990, 1993; Nesbitt & Young, 1996).

Diagenetic redistributions of rare earth elements (REE) are one of the alteration processes that may influence sedimentary successions containing authigenic phases. This process may be associated with preferential assimilation of Middle Rare Earth Elements (MREE) in phosphatic particles. The REE content initially adsorbed on clay minerals and Fe-Mn oxy-hydroxides may be the sources for the latter MREE uptake in phosphates by porewater migration (Lumiste et al., 2023). This fractionation mechanism remains poorly understood, and sedimentary rocks affected by it might yield erroneous Nd model ages that do not accurately represent the mean age of mantle extraction for the provenance components (Milodowski & Zalasiewicz, 1991; Bock et al., 1994; McDaniel et al., 1994; Ehrenberg & Nadeau, 2002).

The Alto Tapajós Basin (ATB) is presently classified as intracratonic, filled with Paleozoic siliciclastic sedimentary rocks (Toczeck et al., 2019), and situated in the southern region of the Amazonian Craton. In this study, we investigate São Benedito Formation successions from ATB, known to contain phosphatic sedimentary rocks. The

goals were to assess the depositional system, tectonic setting, provenance, and evaluate sedimentary/diagenetic processes employing petrography, mineralogy, whole-rock geochemistry, and Nd isotopes. Our findings may contribute to a better understanding of this lesser-explored basin and shed light on the mechanism and sources behind the enrichment of MREE in fluorapatite. Firstly, we evaluated the influence of authigenic minerals and diagenesis on geochemical and isotopic compositions of the sedimentary rocks to further constrain the sediment provenance.

2 Geological Setting

The ATB is located on the southern portion of the Amazonian Craton, between the Tapajós-Parima and Rondônia-Juruena provinces (Santos et al., 2000; Santos, 2003; Santos et al., 2006, 2008), occupying an area of 97,000 km² (Figure 1). Toczeck et al. (2019) define the basin as an intracratonic rift, mainly composed of Paleozoic siliciclastic sedimentary rocks intruded by Mesozoic dyke swarms. The study area is on the northwestern portion of the ATB (Figure 1 C), covering the Precambrian basement rocks of the Juruena Domain (Scandolara et al., 2017) or the Western Amazonia Igneous Belt (Rizzotto et al., 2019).

The rifting that gave rise to the ATB was produced by the reactivation of a precursor rift, where the succession of the Beneficente Group (~1.7 Ga) was deposited. Subsidence of the basin occurred between the Devonian and Permian through passive rifting. During the Jurassic, the ATB experienced a tectonic-thermal event related to the fragmentation of Pangea and the expansion of the Central Atlantic Magmatic Province (CAMP), which led to the intrusion of mafic dike swarms (180 – 220 Ma). In contrast with the Amazon Basin, The ATB has positive relief combined with the absence of Cenozoic deposits, which may indicate regional uplift (Toczeck et al., 2019).

The studied succession is assigned to the São Benedito Formation, composed of interlayered gray to greenish shales/siltstones and quartz-arenites, some of them having phosphate, glauconite, and pyrite (Santiago et al., 1980; Bizinella et al., 1980; N. J. Reis, 2006). The rocks could be related to the Juma Formation too, as defined in Reis (2006), but we give preference to the first nomenclature for its stratigraphic priority. Palynology investigations on the Jatuarana Group (Borrachudo and São Benedito Formations) rendered a Silurian-Devonian age (Bizinella et al., 1980), but more studies are necessary. The depositional system for the unit remains uncertain, but at least there

is agreement of a shallow marine environment (Santiago et al., 1980; Bizinella et al., 1980; N. J. Reis, 2006; N. Reis et al., 2006a; N. J. Reis et al., 2006b; Motta et al., 2016; N. J. Reis et al., 2017; Simões et al., 2021).

The local basement rocks comprise metasedimentary rocks of the Abacaxis Formation (>1.85 Ga), Orosirian granitoids (1.85-1.83 Ga), felsic and subordinate mafic volcanic rocks of the Colíder Group (1.82-1.78 Ga), alkaline to subalkaline Statherian granitoids of the Igarapé das Lontras and Teodósia intrusive suites (1.76-1.75), paragneisses of the Quatro Cachoeiras Complex (~1.75 Ga), volcanic-sedimentary rocks of the Beneficente Group (~1.74 Ga), type-A granitoids of the Serra da Providência Suite (1.57-1.53 Ga), mafic igneous rocks from Mata-Matá Suite (1.57-1.54 Ga), and sedimentary rocks from Prainha Formation (Mesoproterozoic) (Santos et al., 2000; N. J. Reis et al., 2006b; Almeida et al., 2016; Meloni & Filho, 2017; N. J. Reis et al., 2017; Scandolara et al., 2017; Rizzotto et al., 2019; Simões et al., 2020, 2021; Albuquerque et al., 2023).

According to Albuquerque et al. (2023), the Borrachudo and São Benedito Formations from ATB, have major sediment contributions from the local basement of the Rondônia-Juruena Province (U-Pb in zircon: 1.82-1.54 Ga; T_{DM}: 3.50-1.60 Ga), more specifically from Colíder Group, Statherian granitoids/gneiss, Pedro Sara Formation, and the recycling of Beneficente Group and Prainha Formation sedimentary rocks.

3 Materials and Methods

This study is based on medium to fine-grained sandstones, mudstones, and marls from three drill core successions of the extreme northwestern portion of ATB (Figure 2). Sampling considered whole-depth coverage, avoidance of weathered samples, and all the range of lithofacies. Thin sections were made to determine the composition, texture, classify the rocks, conduct the study of authigenic minerals, and give tectonic and provenance first insights.

WDS mineral chemistry analyses of thin sections were carried out in the Electron Microprobe Laboratory at the University of Brasília, Brazil, using a JEOL-JXA-8230 instrument. Analytical conditions included a bombarding voltage between 15 and 20 kV, a current of 2×10^{-8} A, and a beam diameter of 1 μm. For each analyzed element, calibrations were performed on standards with known concentrations. The analyses

aimed to determine the composition of glauconitic minerals, phosphates, and carbonates. The content of rare earth elements was determined qualitatively.

Samples were ground and homogenized by a tungsten carbide disc mill. The powder of each sample was used for X-ray diffraction analysis, elemental and Nd isotopic geochemistry. X-ray diffraction analyses were performed to determine bulk mineralogy of the samples. The instrument was a Rigaku Ultima IV instrument (X-ray Diffractometry Laboratory, University of Brasília) with copper Kα radiation filtered by Ni, a 35 kV voltage, and a 15 mA current. The samples were scanned from 2-60°, with 0.05° of step size and 5°/min scan speed. Interpretation of the diffractograms was carried out using MDI/Jade® 9 software.

Whole-rock geochemical analyses were conducted by the ALS Global laboratory in Lima, Peru. For major oxides (SiO_2, Al_2O_3, Fe_2O_3, CaO, K_2O, MgO, Na_2O, K_2O, TiO_2, MnO, P_2O_5, LOI), rare earth elements, and trace elements (Ba, Ce, Cr, Cs, Dy, Er, Eu, Ga, Gd, Hf, Ho, La, Lu, Nb, Nd, Pr, Rb, Sm, Sn, Sr, Ta, Tb, Th, Tm, U, V, W, Y, Yb, Zr), powdered samples were fused with lithium meta- and tetraborate, and the resulting melt was acid dissolved. Major oxides were determined by ICP-AES and trace elements were determined by ICP-MS. Base metals (Ag, As, Cd, Co, Cu, Li, Mo, Ni, Pb, Sc, Tl, and Zn) were determined by four-acid digestion and analyzed by ICP-AES.

The Chemical Index of Alteration (Nesbitt & Young, 1982) was calculated by:

$$CIA = [A/(A + C^* + N + K)]x100;$$

in which, the letters are for the molecular proportions of $A = Al_2O_3$, $C^* = CaO$ (corrected for phosphates and carbonates), $N = Na_2O$, and $K = K_2O$. Since C* was higher than N on all samples, N was used as representing C.

To remove the Oddo-Harkins effect on diagrams, REE and other trace elements were normalized to UCC (Upper Continental Crust) using the values of Mclennan (2001). Particularly, values of Cl chondrite from Pourmand et al. (2012) were utilized to calculate the ratios $(La/Sm)_N$ and $(Gd/Yb)_N$, to further construct the Bock et al. (1994) diagram to evaluate sorting or REE redistribution.

Nd Isotope analysis was performed using a Thermo Scientific TRITON Plus thermal ionization mass spectrometer at the Laboratory of Geodynamic, Geochronological, and Environmental Studies (LEGGA), Institute of Geosciences (IG), University of Brasília (UnB). Sample preparation, digestion, and Nd isotope extraction followed the procedures described in Gioia and Pimentel (2000). The data were corrected for fractionation using $^{146}Nd/^{144}Nd = 0.7219$. Validation of the results was

performed using the BHVO-2 reference material, which yielded $^{143}Nd/^{144}Nd$ = 0.513008 ± 0.000007 (2SE) and 0.513002±0.000019. For εNd(t) and $f_{Sm/Nd}$ calculations, it was used $^{147}Sm/^{144}Nd_{(0)}$ = 0.1960 and $^{143}Nd/^{144}Nd_{(0)}$ = 0.512630 as CHUR ratios (Bouvier et al., 2008). For depleted mantle model ages (T_{DM}) it was used εNd(t) = $0.25T^2$ - 3T +8.5 as the DM evolution curve (DePaolo, 1981).

4 RESULTS

4.1 Petrography

The studied drill cores can be divided into a sandy-muddy part to the top and a muddy dolomitic to the base (Figure 2). The first one is composed of fine to medium and rarely coarse-grained sandstones interbedded with mudstones and rare breccias horizons of angular sandstone fragments (Figure 3). The basal muddy-dolomitic succession is composed of mudstones, dolomitic mudstones, marls, dolostones, and carbonate breccias (Figure 3). These lithofacies are detailed from proximal to distal (Table 1).

4.1.1 Sandstones

The sandstone beds are centimetric to decametric, light to dark gray, medium to very fine-grained, and moderately to well sorted with mostly subrounded grains. The coarser-grained beds commonly have sandstone and mudstone fragments on their base. The beds are apparently massive or have planar to wavy laminations, and low-angle cross-laminations. Some of the topmost beds have symmetric ripples at the top (Figure 4 A).

The sandstones are compositionally classified as quartz-arenites, except for some of the topmost beds, where subarkoses often occur (Figure 3). The quartz grains always have quartz overgrowths. Microcline is the most common feldspar and plagioclase is rare. The authigenic components show some reworking features and are mostly composed of fluorapatite, glauconite, and siderite. Fluorapatite occurs as peloids, ooids, intraclasts, cements, coatings on detrital grains, and as fragments of hardgrounds. Glauconite occurs as peloids, cements, coatings, and in composite intraclasts with fluorapatite. Siderite occurs often as intergranular cement and ooids, mainly on the topmost beds. There are fluorapatite grains included or coated by glauconite (Figure 5 B, C, D), grains of glauconite aggregates with gradual transitions to fluorapatite at the borders (Figure 4 A), and intraclasts composed of mixtures of both minerals (Figure 5

D, F, G, J). White micas, pyrite, sideritic ooids, chert, and zircon are common accessory components (Figure 5).

4.1.2 Sandstone with mudstone interbeds

Some intervals are composed of centimetric sandstone beds with mudstone interbeds of millimeters up to 2-3 cm thick (Figure 3 G e D). Their main structure is planar to wavy laminations, and secondarily, low-angle cross-laminations with mud-drapes and truncations. Some of the cross-laminations seem to be hummocky cross-stratifications (Figure 4 C, D), but their identification is limited on drill cores. There are commonly normal-graded beds of sandstones to mudstones, ending on sharp planar or erosive contacts (Figure 4 B). Soft-sediment deformation structures, like fluid injection/escape structures, disturbances of the laminations, and convolute beddings, are common (Figure 4 E, F, G, H, I).

4.1.3 Mudstones

The mudstones include dark-colored siltstones and black shales (Figure 3 E). They normally show planar laminations or are massive and composed of quartz, feldspars (normally microcline), illite (clay fraction mica), white micas (probably muscovite), kaolinite, fluorapatite (Figure 5 F), pyrite (Figure 5 I, L), and organic matter. Some mudstone beds presented rice-grain-shaped siderite.

4.1.4 Marls and dolostones

The light gray to white marls and impure dolostones from the basal succession (Figure 3 H, I) are massive or present planar laminations with some soft-sediment deformation structures (Figure 4 E, H, I). They are interbedded in sharp or gradual contact with mudstones, especially lighter-colored dolomitic mudstone intervals. The marls and dolostones are composed essentially of fine crystals of dolomite (possibly recrystallized micrite/dolomicrite) and the same mineral phases as the mudstones.

4.1.5 Breccias

The succession also presents some breccias up to 20 cm thick. They are made of sandstone fragments on the upper terrigenous portion, and carbonate intraclasts on the basal portion (Figure 3 F, J).

4.2 Mineral Chemistry

Electron microprobe analysis was conducted on the authigenic phases to confirm their existence and evaluate contributions to whole-rock geochemistry. Analysis of

phosphatic components (Table 2) indicates fluorapatite as the only phosphate, probably the francolite variety, for presenting more than 2 atoms per formula unit of F. The fluorapatite mineral formula based on 25 O, Cl, and F is $Ca_{9.57}Na_{0.13}Mg_{0.03}Al_{0.02}Fe_{0.12}Mn_{0.02}K_{0.02}(PO_4, CO_3, SO_4)_6F_{2\text{-}3}$. Glauconitic minerals (Table 3) are dioctahedral interlayer deficient micas/illites, Fe and K-rich, and have higher Al contents compared to glauconites *stricto sensu*. The K_2O contents between 6 and 8 % indicate an evolved stage glauconitic mineral (Odin & Matter, 1981; Amorosi et al., 2007). The glauconitic mineral formula based on 11 O, OH, F, Cl, and FeO as the total iron content is $K_{0.70}Na_{0.02}Ca_{0.02}(Al_{1.03}Ti_{0.01}Fe_{0.55}Mg_{0.56})(Si_{3.86}Al_{0.14})O_{10}(OH_{1.77}F_{0.23})$. Siderite ooids and cement present compositions of Mg-siderite (Table 4). The siderite mineral formula calculated based on 6 O is $Fe_{1.23}Mg_{0.66}Mn_{0.08}Ca_{0.03}(CO_3)_2$.

4.3 Geochemistry

4.3.1 Major elements

The geochemical data are given in Table 5. Four lithogeochemistry groups are defined by the major elements: sandstones, Fe-sandstones, mudstones, and marls. Sandstones are characterized by the highest grades of SiO_2 (78.60-94.10 wt.%). Fe-sandstones have higher grades of Fe_2O_3 (9.76-11.57 wt.%), MnO (0.44-0.74 wt.%), and MgO (1.76-4.28 wt.%). Some samples of the two groups could be classified as phosphatic sandstones, due to P_2O_5 content between 2.52 and 5.09 wt.%. Mudstones have the highest Al_2O_3 (7.75-20.00 wt.%) and K_2O (6.10-9.10 wt.%) contents. Marls have the highest CaO (9.11-11.09 wt.%), MgO (5.27-6.94 wt.%), and LOI (15.20-25.20 wt.%) contents and the lowest SiO_2 (31.50-57.90 wt.%). All lithogeochemistry groups have low values of Na_2O.

Based on the UCC-normalized diagrams (Figure 6 A, B) all sample groups are enriched on P_2O_5 and depleted on Na_2O. Sandstones are depleted in Al_2O_3, Fe_2O_3, and MgO. The normalized MnO, CaO, and K_2O vary greatly but are depleted on average. Fe-sandstones are enriched in Fe_2O_3, MnO, MgO, P_2O_5, and depleted in Al_2O_3 and K_2O. Mudstones are the less uniform group, but on average Al_2O_3, Fe_2O_3, MnO, MgO, and K_2O values are closer to the UCC composition. Marls are enriched in MnO, MgO, and CaO.

The discriminant function analysis diagrams based on the composition of the major elements, used to evaluate the tectonic setting (Verma & Armstrong-Altrin, 2013)

show samples mainly on the rift and some on the collisional field (Figure 8 A, B). The discrimination diagram for provenance signatures (Roser & Korsch, 1988) indicates a recycled provenance source (Figure 8 C), and all samples, except marls, plot within the passive margin field of Roser and Korsch (1986) bivariate diagram (Figure 8 D).

CIA values varied between 67.80 and 48.31 (Table 5). On the A-CN-K ternary plot (Nesbitt & Young, 1984) the data plots mainly on the A-K axis near the K-feldspar composition (Figure 8 E).

4.3.2 Trace elements

Compared to UCC, all sample groups show similar patterns, which are associated with the source area chemistry control of these rocks. Exceptions are the higher enrichments of Pb and Ta on sandstones and Fe-sandstones. Mudstones are more enriched in trace elements on average (Table 6). Large ion lithophile elements (Rb, Ba, Sr) contents are low but variable and some mudstones show Rb enrichments (Figure 6 C, D). The high field strength elements (Th, U, Zr, Hf) vary from enriched to depleted, but most of the sandstones are depleted on Zr and Hf. Y concentrations are close to the UCC values in all samples. Sc, V, and transition metals (Cr, Cu, Ni, Zn) are overall depleted and some of the mudstones and marls have Zn enrichments.

The bivariate diagrams that compare incompatible (Th and Zr) with compatible (Sc and Ti) elements indicate provenance from felsic to intermediate sources (Figure 9 A, B). The diagram of Th/Sc vs. Zr/Sc (McLennan, 1993) shows a sediment recycling/sorting/zircon addition trend for all samples (Figure 9 C). The samples plot mainly within the passive margin and continental island arc fields of the Th-Zr/10-Sc ternary diagram (Bathia and Crook, 1986 - Figure 9 D).

4.3.3 Rare-earth elements (REE)

In general, sandstones and Fe-sandstones show similar total REE and LREE contents, while mudstones have the highest and marlstones have the lowest contents (Table 7). All sample groups show similar total HREE contents, but marls show slightly lower values. Some of the sandstones and Fe-sandstones show much lower $(La/Sm)_N$ and higher $(Gd/Yb)_N$ values in comparison to the mudstones and marls.

Four main patterns can be individualized on the REE normalized diagrams. The sandstones have slight LREE depletions relative to the HREE, and MREE enrichments (Figure 7 A). The Fe-sandstones have LREE depletions and pronounced MREE enrichments, forming bell-shaped patterns (Figure 7 C). Most of the mudstones and

marls have overall flat patterns (Figure 7 B), but the samples L4F3 51.25, L10F0 9.87, and L10F0 28.26 have slight concave up patterns, with MREE depletions (Figure 7 D).

4.3.4 Nd Isotopes

The Nd isotope analysis is shown in Table 9 and Figure 10. As the deposition ages of the studied rocks remain uncertain, we used a conservative estimate of t = 0.42 Ga for εNd(t) calculations. In general, sandstones (9 samples) and Fe-sandstones (3 samples) yield the highest values of $f_{Sm/Nd}$ (-0.59 to 0.01), ƐNd(t) (-21.95 to -8.32), and T_{DM} (2.12 – 5.25 Ga). Mudstones (4 samples) and marls (4 samples) have similar lower values of $f_{Sm/Nd}$ (-0.54 to -0.32), ƐNd(t) (-21.64 to -15.71), and T_{DM} (2.24 – 2.76 Ga) (Table 9).

Exceptionally, three fine-grained samples yielded different results. One marl sample, from the FE6 drill core at a depth of 55.15 m, exhibits $f_{Sm/Nd}$ of -0.41, an anomalously negative εNd(t) value of -29.19, and a much older T_{DM} of 3.35 Ga. Other marl sample, FE6 46.27, have values of - $f_{Sm/Nd}$ = -0.22, ƐNd(t) = - 12.09, and T_{DM} = 2.92. At last, one mudstone, sample L10F0 28.26 gave values of - $f_{Sm/Nd}$ = -0.54, ƐNd(t) = - 0.92, and T_{DM} = 0.92.

5 DISCUSSION

5.1 Depositional System

The studied succession is interpreted as deposited on a shallow marine environment by previous works (Santiago et al., 1980; Bizinella et al., 1980; Reis, 2006; Reis et al., 2006a, 2006b; Motta et al., 2016; Reis et al., 2017; Simões et al., 2021), possibly on a regressive storm-dominated shelf, from the outer shelf to the lower shoreface (Figure 11). The prograding succession and aggrading interbedded interval may indicate a Highstand System Tract (HST). The terrigenous portion was deposited mainly by fair-weather/storm waves and currents (combined flow), followed by suspended load settling at background conditions. The muddy-carbonate (hemipelagic?) part was deposited by suspended load settling and the carbonate intervals suggest periods of minor terrigenous influx to the system. The breccias could be related to

tectonism/seismicity (Motta et al., 2016). The soft-sediment deformation structures were probably formed by liquefaction and overloading during tectonism/seismicity or induced by storm rapid deposition (Molina et al., 1998). The lack of bioturbation and benthonic fossils may be related to anoxic conditions.

Although the authigenic components in the study succession show reworking features, the presence of Siderite, glauconite, fluorapatite, pyrite, and dolomite are also indicative of inner to outer shelf deposition and would require slow rates of sedimentation, at least during intervals of background conditions (Glenn & Arthur, 1988; Föllmi, 1996; Pufahl & Grimm, 2003; Mücke, 2006; Pufahl & Groat, 2017; Vuillemin et al., 2019; López-Quirós et al., 2020; Chang et al., 2022). The *in situ* primary phosphate particles on the basal mudstones and marls (Figure 5 F) suggest that initially, phosphogenesis occurred on the outer shelf, accompanied by pyrite and carbonate formation. During progradation, under the prevalence of sub-oxic conditions, it started glauconite formation on the inner shelf. Finally, on the near-shore lower part, there would mainly be siderite formation, that could have involved the substitution of chamosite and hematite. The reduction of oxyhydroxides could potentially be one of the sources of Fe to form siderite and P and REE that would later compose the phosphate particles, but the gathered data lacks evidence to support this hypothesis. The action of storm waves and currents eroded, reworked, and transported the authigenic components, concentrating and putting them in contact, even though they probably formed under distinct parts of the shelf, oxic-anoxic conditions, and depths of the sediment pile (Glenn & Arthur, 1988; Pufahl & Groat, 2017; El Bamiki et al., 2023).

The Phanerozoic-like phosphatic particles (dark to pale brown and cryptocrystalline/pseudo-isotropic grains - Figure 5) and the presence of other marine phases confirm that most of the phosphate content is authigenic. Phosphorus is delivered via weathering of continental rocks to the ocean in dissolved or particulate forms. Dissolved P species are readily available for biological uptake, but most particulate P consists of insoluble igneous and metamorphic phosphatic minerals that never participate in the cycling (Föllmi, 1996; Pufahl & Groat, 2017). The possible sources of P in our context are the degradation of organic matter and the release of adsorbed P from clays and oxyhydroxides.

The dolomite content in the marls and dolostones might represent a primary occurrence, supported by depth-related mineral paragenesis, its occurrence within a predominantly siliciclastic succession, and the absence of calcite content. The dolomite

formation likely took place under the influence of microbial activity at the sulfate/methane boundary (Meister et al., 2007). Recent findings suggest that dolomite can form at ambient conditions, where cycles of saturation and undersaturation dissolve cation-disordered surfaces and reprecipitate increasingly ordered crystals, enabling and accelerating dolomite primary growth (Kim et al., 2023). The dolomite content found on the Peruvian shelf was interpreted by some as primary and not substituting precursors carbonate phases and is associated with other authigenic minerals like phosphate, glauconite, and pyrite (Glenn & Arthur, 1988; Jørgensen et al., 2006; Meister et al., 2007).

5.2 Sedimentary and Diagenetic Processes

Firstly, to evaluate provenance it's necessary to make sure that the results reflect a continental signal. Based on the whole-rock geochemical and EMPA data (Tables 2, 3, and 4), the authigenic minerals formed on the sediment/water interface and during diagenesis significantly influenced the sandstones whole-rock compositions, adding mainly Fe_2O_3, MnO, CaO, MgO, K_2O, and P_2O_5. Despite the marine phases, the source signature of the sandstones remains observable. This is evident through the immobile trace elements, which exhibit similar ratios compared to the mudstones and marls. Additionally, their concentrations positively correlate with the Al/Si ratio (Table 8).

The CIA was created to help interpret paleoclimatic conditions by measuring the degree of weathering at the sediment source area, but sorting and diagenetic processes can significantly change it (Nesbitt & Young, 1982, 1989). The data trend on the A-CN-K ternary diagram revealed that hydraulic sorting or diagenesis could have impacted the index by K-addition, probably due to the abundance of microcline, the presence of glauconitic minerals, or the two combined (Figure 8 E). Thus, the sample's lower CIA values do not necessarily indicate a proximal primary source or the influence of an arid/cold climate.

REE patterns are useful for evaluating provenance and fractionating sedimentary processes such as weathering, sorting, and diagenesis. Based on the marine authigenic phases present on the samples, the bell-shaped REE patterns of the sandstones reflect marine pore water signatures stored on phosphatic particles (Haley et al., 2004; Chen et al., 2015; Tostevin et al., 2016; Lumiste et al., 2023). The REE model for marine pore waters from Haley et al. (2004) discusses that this pattern is due to Fe-oxyhydroxides reduction under anoxic conditions. The MREE enrichments could be related to a

previous Fe-oxyhydroxides content substituted by siderite under the anoxic conditions since the iron-rich samples have the greatest MREE enrichments.

Normally diagenesis is believed to not affect significantly REE composition. However, some studies indicate that under certain conditions REEs can be redistributed through sedimentary successions (McLennan et al., 1993; Bock et al., 1994; McDaniel et al., 1994). The slightly MREE-depleted patterns in some mudstones (Figure 7 D), contrasting with the inverse pattern of sandstones and Fe-sandstones (Figure 7 A, C), suggests that the fluorapatite uptake of REE also occurred from desorption from fine-grained horizons in interbedded intervals. The mudstone sample L10F0 28.26 m has a MREE depletion and rendered a much younger T_{DM} compared to all other results. These features could support REE mobilization through the succession, considering that in the compiled data for the possible source rocks, there is no similar result, and the loss of MREE adsorbed on clay-minerals probably disturbed the Sm-Nd system (Figure 10).

Since all samples that have Sm/Nd ratios ≥ 0.23 present a higher T_{DM} and together form an almost vertical distribution on the $f_{Sm/Nd}$ vs. εNd(t) diagram (Figures 10 A, B), they are considered not to reproduce the weighted average crustal residence time of the siliciclastic sediment sources (Bock et al., 1994; Ehrenberg & Nadeau, 2002). These samples (most of the sandstones and one marl) are not considered for the provenance analysis. On the $f_{Sm/Nd}$ vs. εNd(t) diagram the sandstones show a nearly vertical distribution, showing that at the approximate time of deposition, the samples had a similar εNd(t).

5.3 Sedimentary Provenance and Tectonic Implications

Compared with UCC, the analyzed samples exhibit primarily felsic characteristics due to depletions in Ti, Na, Sc, V, and transition metals (Figure 6 C D) (McLennan et al., 1993). The higher depletion of HFSE in sandstones compared to mudstones is likely due to dilution owing to higher quartz content (McLennan et al., 1990). Trace element diagrams do not indicate source differences based on grain size. Therefore, from a trace element perspective, sandstones, mudstones, and marls share the same terrigenous source nature.

No evidence from major and trace elements geochemistry that would justify a possible juvenile mafic source component, which can have the same effect on the sandstone isotopic results.

No evidence in major trace element geochemistry would justify a different source component for all samples.

The negative εNd(t) range values suggest a main old upper continental crust (OUCC) provenance for the samples (Figure 10 C). Sedimentary rocks with high Th/Sc ratios, low $f_{Sm/Nd,}$ and εNd(t) values are interpreted to originate from OUCC or are recycled from sedimentary rocks that are typically found in passive margins or intracratonic settings (McLennan et al., 1993).

Almost all fine-grained rock Sm-Nd isotopic results ($f_{Sm/Nd}$ = -0.54 to -0.32; ƐNd(t) = -21.64 to -15.71) fall between the fields of Rondônia-Juruena and Tapajós-Parima provinces (Figure 10 D). Although the results are ambiguous between the two provinces, on a local scale, they align with the value ranges of the Colíder Group and chrono-correlated plutonic suites, similar to the results for ATB rocks from Albuquerque et al. (2023). The evidence of sediment recycling (Figure 9 C) indicates provenance from the reworking of the underlying Beneficente Group sedimentary succession. One marl isotopic result rendered a possible change in sediment contribution for the São Benedito Formation when compared to other results from this study and Albuquerque et al. (2023). The anomalous value (T_{DM} = 3.35 Ga; εNd(t) = -29.19) may be related to unknown/non-outcropping rocks or maybe to a more distant contribution from Central Amazon Province rocks.

Based on the discriminant function analysis diagrams (Figures 8 and 9 D), along with the high textural maturity, evolved major element compositions, and Nd isotope results, it is most probable that the successions originate from a passive margin. So, the petrographic and geochemical results support the interpretations of Toczeck et al. (2019) and earlier studies that classified the basin as an intracratonic rift, supported by structural-geophysical data, its elongated form, and location.

The continental island arc characteristics observed in some samples (Figure 9 D) and the collisional field plot for the less mature ones (Figure 8 B) are attributed to their inheritance from the Beneficente Group or the influence of authigenic marine phases on the whole-rock composition. Albuquerque et al. (2023) argue that the continental island arc and active continental margin signatures observed on Beneficente Group are due to the arc-related basements of Tapajós-Parima and Rondônia-Juruena. So, considering the reworking of Beneficente Group as one of the main sediment sources for the studied rocks, the collisional plot may be also inherited.

6 CONCLUSIONS

The data presented above allow us to conclude that:

●The studied São Benedito Formation succession was deposited in a shallow marine environment, most probably on a regressive storm-dominated shelf. The depth-related authigenic mineral paragenesis (Siderite, glauconite, fluorapatite, pyrite, and dolomite) and lithofacies interpretations suggest overall anoxic conditions and deposition from outer to inner shelf and lower shoreface.

●Mainly coarse-grained samples have their Nd isotopic compositions influenced by marine authigenic phases and can't be used for provenance. The continental/siliciclastic Nd isotopic signature is contaminated by marine pore water signatures stored on fluorapatite. The mechanism of enrichment may be linked to the reduction of Fe species and the MREE depletions on some of the mudstones, which probably are the initial REE sources for the uptake of fluorapatite. One mudstone sample that has a MREE depletion coupled with a much younger T_{DM} of 0.92 Ga, probably confirms REE redistribution. This result is different from any other of the compiled data for the region and the Amazon Craton.

●Major and trace element compositions indicate mainly felsic sources contributing to the terrigenous sediment budget and a strong sediment recycling component for the studied samples. The T_{DM} and εNd(t) values from mudstones and marls show that the Colíder Group, chrono-correlated plutonic suites, Pedro Sara Formation, and the recycling of the sedimentary succession from Beneficente Group are the main sediment sources for the São Benedito Formation successions, at least on the northwestern portion of the Alto Tapajós Basin. One marl sample yielded a much older T_{DM} of 3.35 Ga and εNd(t) of -29.19, which could indicate a distal source contribution from Central Amazon Province or unknown rocks.

Acknowledgments

7 FIGURES

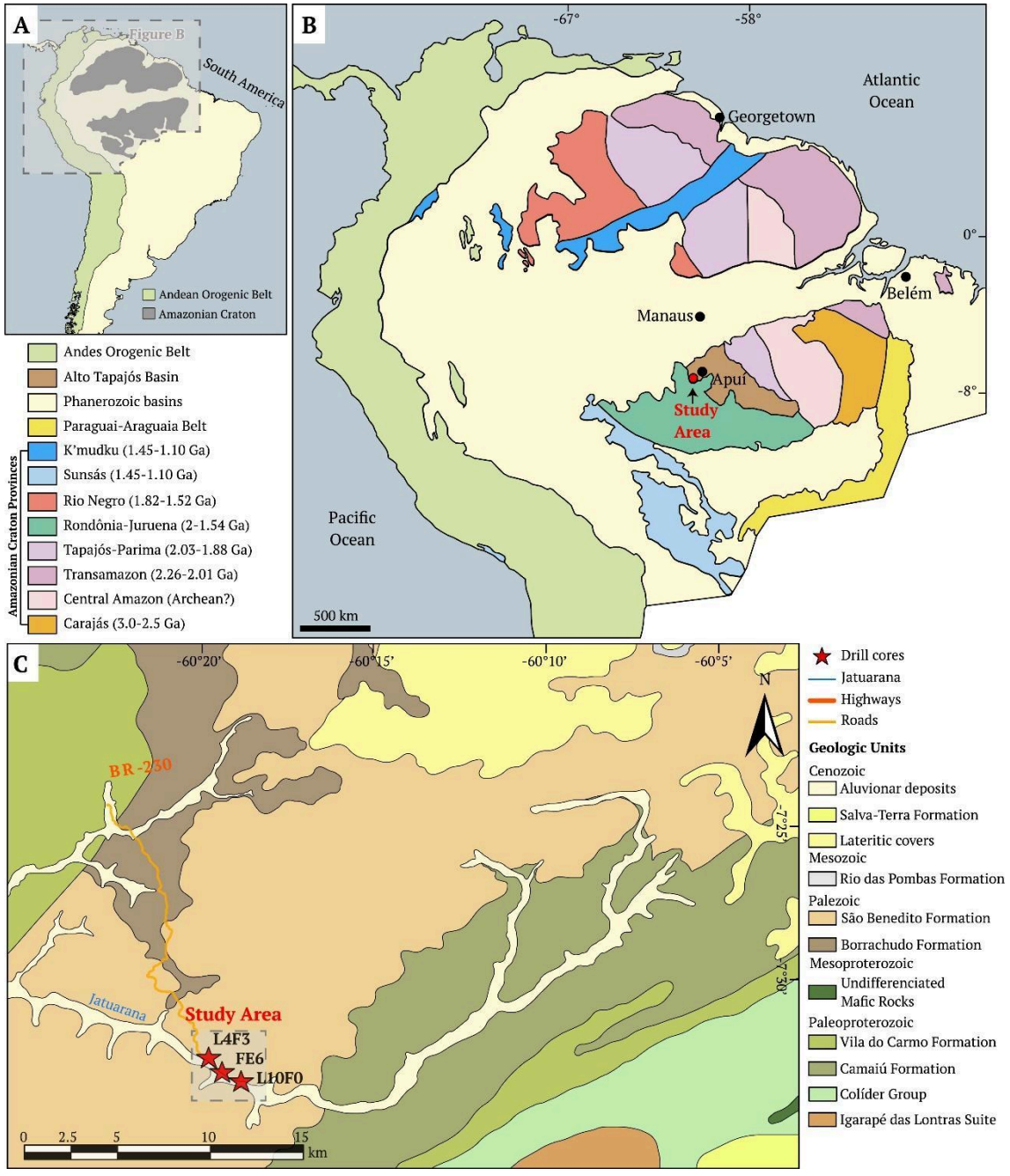

Figure 1: A – Map showing South America, the Andean Orogenic Belt, and the Amazonian Craton contours. B – Map showing the studied area location relative to the geochronological provinces of the Amazonian Craton (Santos et al., 2008) and Alto Tapajós Basin. C – Geological map showing the studied drill cores locations (units after CPRM, 2019?).

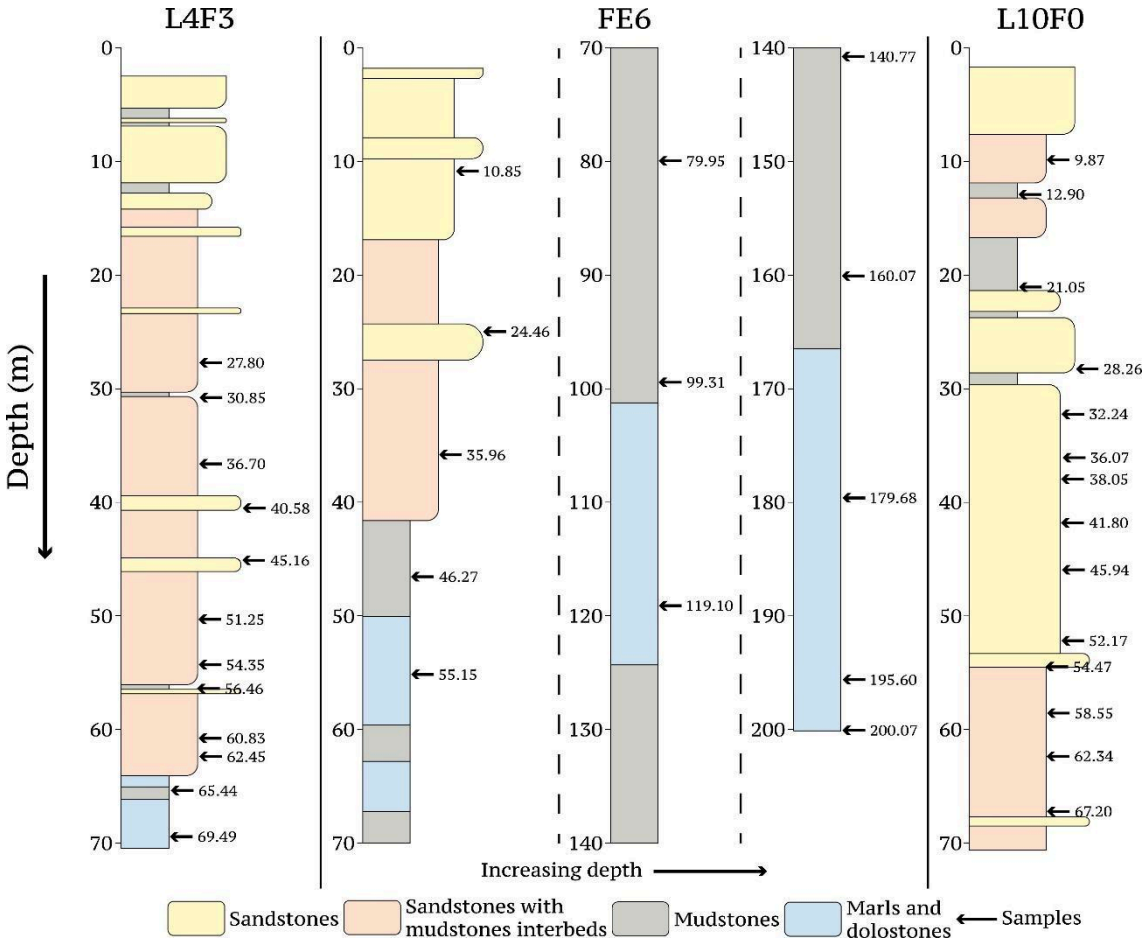

Figure 2: Sedimentary logs of the studied drill cores. Green arrows mark the positions of analyzed samples for whole-rock geochemistry and Nd isotopes. Black arrows mark the positions of analyzed samples just for geochemistry.

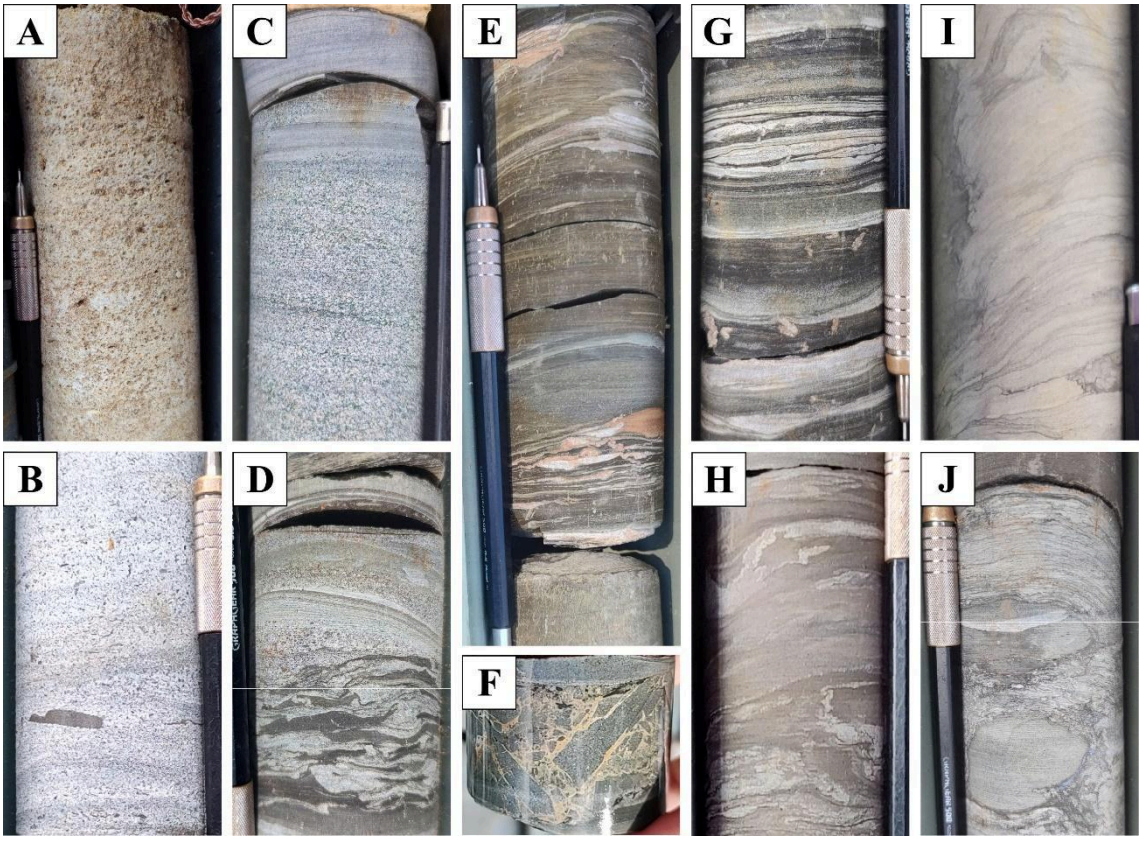

Figure 3: A – L4F2 drill core, depth of 5,50 m, Subarkose; B – L8F-1 drill core, depth of 29,90 m, sandstones bed with shale fragment; C – L10F0 drill core, depth of 68,40 m, normal-graded glauconitic sandstone; D – L4F3 drill core, depth of 33,30 m, interbedded and disturbed sandstone and siltstone; E –L10F0 drill core, depth of 17,50 m, Mudstone with sandy laminations; F – L10F-1 drill core, depth of 32,50 m, breccia composed of sandstone fragments and siderite cement; G – L5F2 drill core, depth of 46,30 m, sandstones and mudstones interbedded; H – L8F-1 drill core, depth of 69,77 m, dolomitic mudstone; I – L4F1 drill core, depth of 22,50 m, dolostone; J – L4F0 drill core, depth of 20,85 m, carbonate breccia.

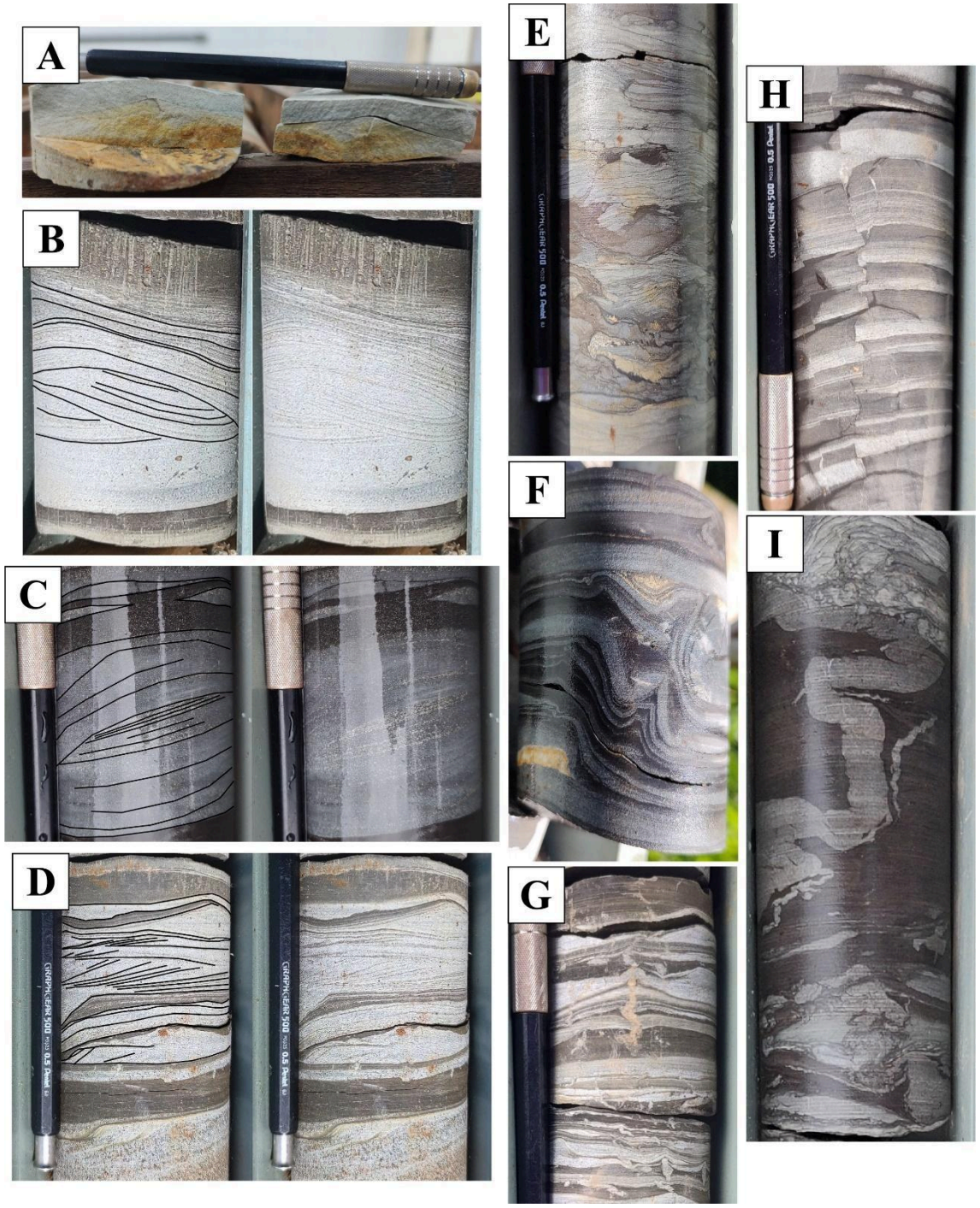

Figure 4: A – FE6 drill core, depth of 7,80 m, symmetrical ripple; B – L4F3 drill core, depth of 34,70 m, hummocky cross-lamination; C – L8F3 drill core, depth of 61,65 m, hummocky cross-lamination; D – L4F3 drill core, depth of 32, 20 m, low-angle truncated cross-lamination; E – L4F2 drill core, depth of 41,05 m, lamination disturbances; F – L8F2 drill core, depth of 70,55 m, convolute lamination; G – L8F-1 drill core, depth of 21,15 m, injection/escape fluid structures; H – L4F1 drill core, depth of 14,50 m, syn-sedimentary fault; I – L8F3 drill core, depth of 68,20 m, ichnofossil and bioturbated strata.

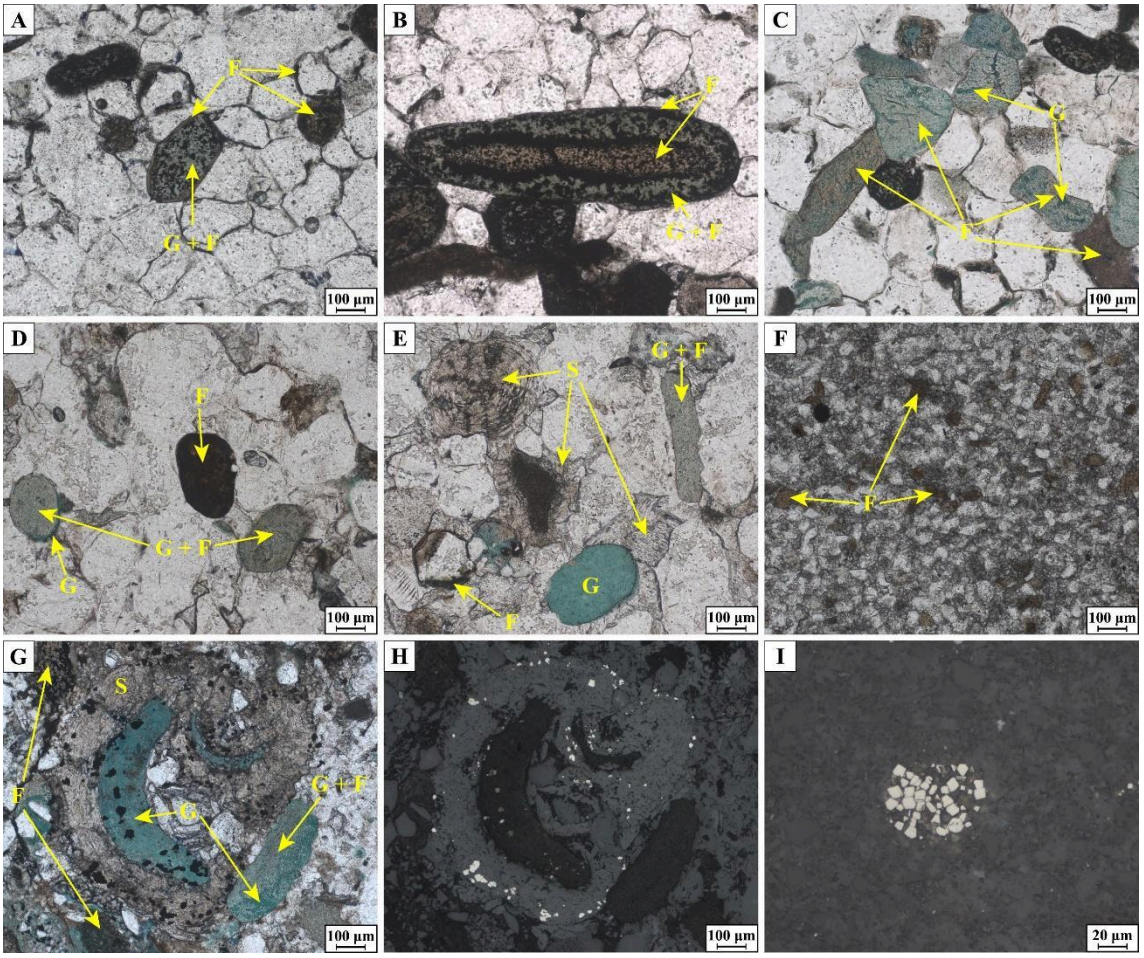

Figure 5: A – L4F3 drill core, depth of 36,70 m, phosphate-glauconite intraclast with phosphate coating, at the center; B – L4F3 drill core, depth of 36,70 m, intraclast of phosphate nucleus with phosphate-glauconite border; C – L4F3 drill core, depth of 45,16 m, mainly phosphate peloids with cracks filled by glauconite; D – L10F0 drill core, depth of 67,20 m, phosphate peloid at the center, and phosphate-glauconite peloids; E – L10F0 drill core, depth of 67,20 m, siderite ooids and cement, glauconite, and phosphate-glauconite peloids; F – FE6 drill core, depth of 195,60 m, *in situ* phosphate particles; G e H – L4F3 drill core, depth of 56,46 m, siderite ooid with glauconite nucleus, both with sub- to euhedral pyrite inclusions; I – L4F3 drill core, depth of 65,44 m, framboidal pyrite. Obs.: Photomicrographs A to G were taken under transmitted light and parallel Nichols. Photomicrographs H and I were taken under reflected light and parallel nichols. Yellow labels indicate, respectively: F – phosphate components; G+F – phosphate-gluconite components; G – glauconite components; and S – siderite components.

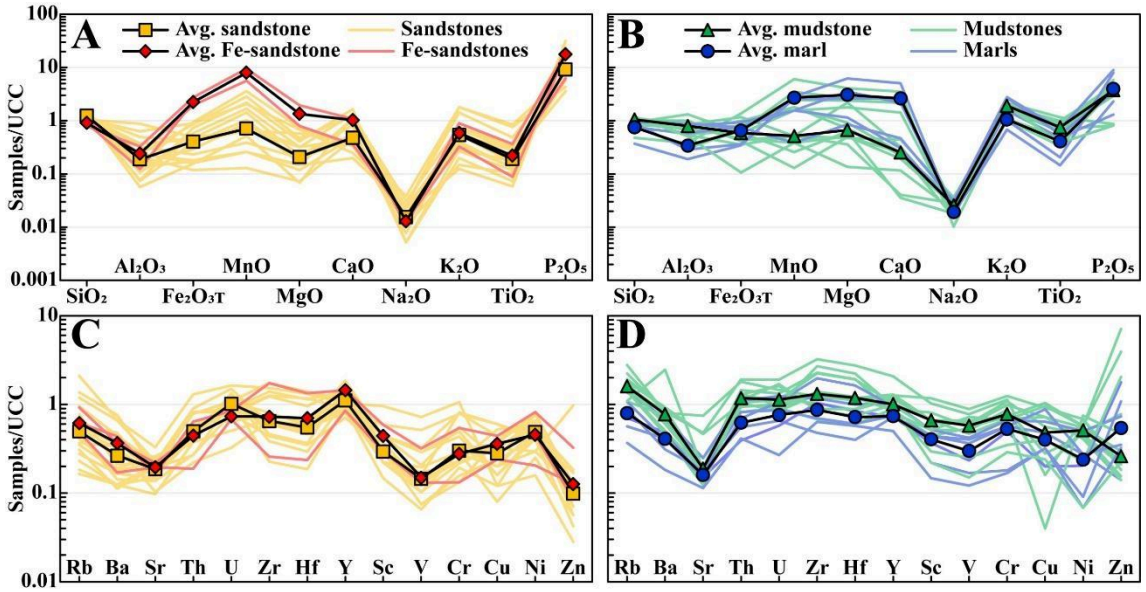

Figure 6: Upper Continental Crust – UCC (McLennan, 2001) normalized diagrams for A-B major, C-D selected trace elements.

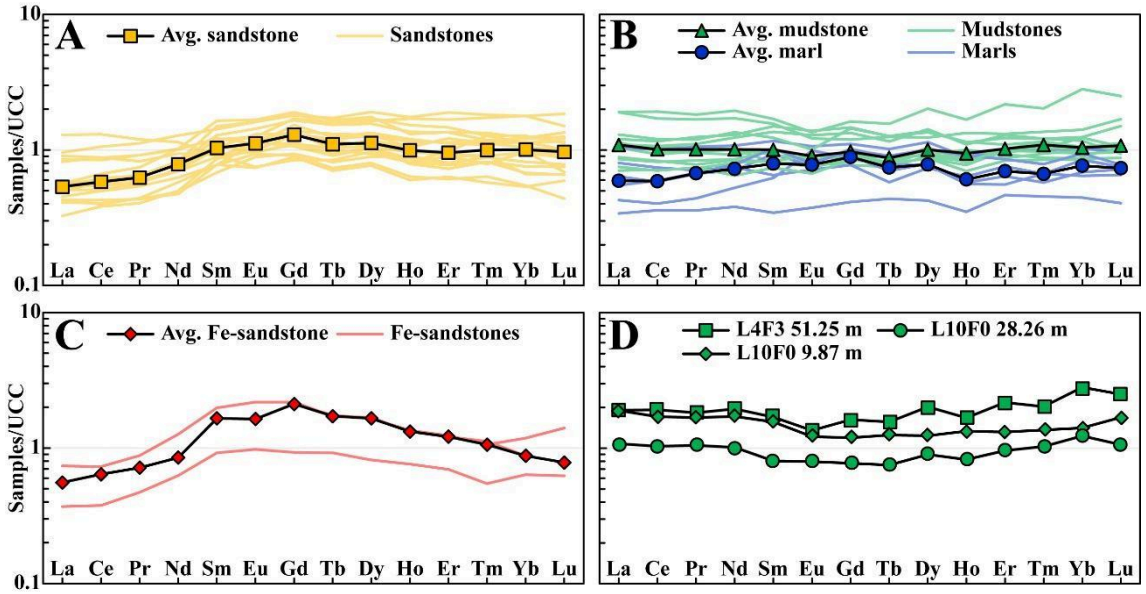

Figure 7: UCC normalized REE diagrams for A – sandstones, B – mudstones and marls, C – Fe-sandstones, D – selected mudstones samples.

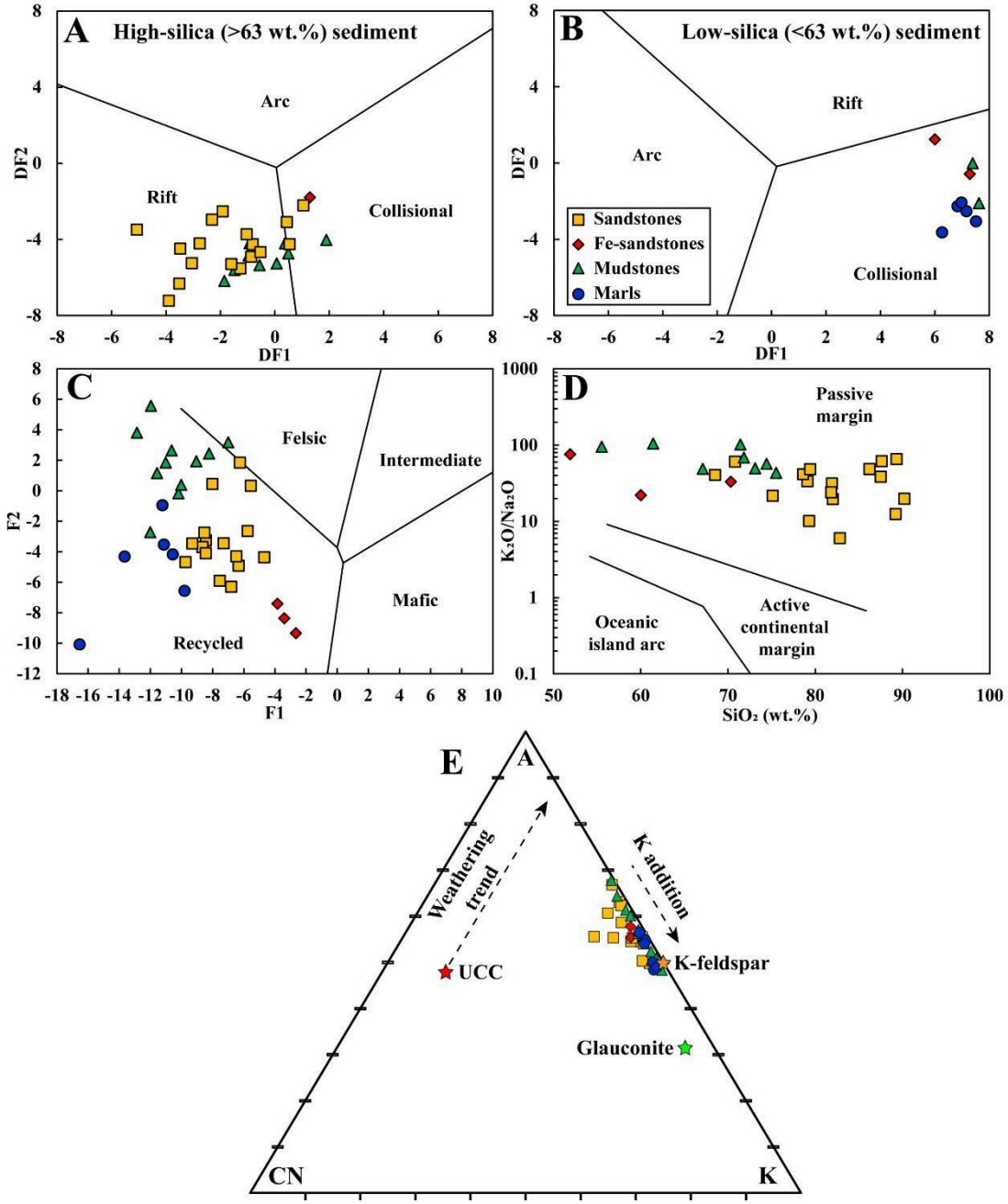

Figure 8: Discriminant function analysis diagrams using major elements data of sedimentary rocks, A-B for tectonic setting discrimination (Verma & Armstrong-Altrin, 2013), C for provenance signatures (Roser & Korsch, 1988); D K_2O/Na_2O vs. SiO_2 diagram for tectonic setting discrimination (Roser & Korsch, 1986); and E – A-CN-K ternary plot (Nesbitt & Young, 1984).

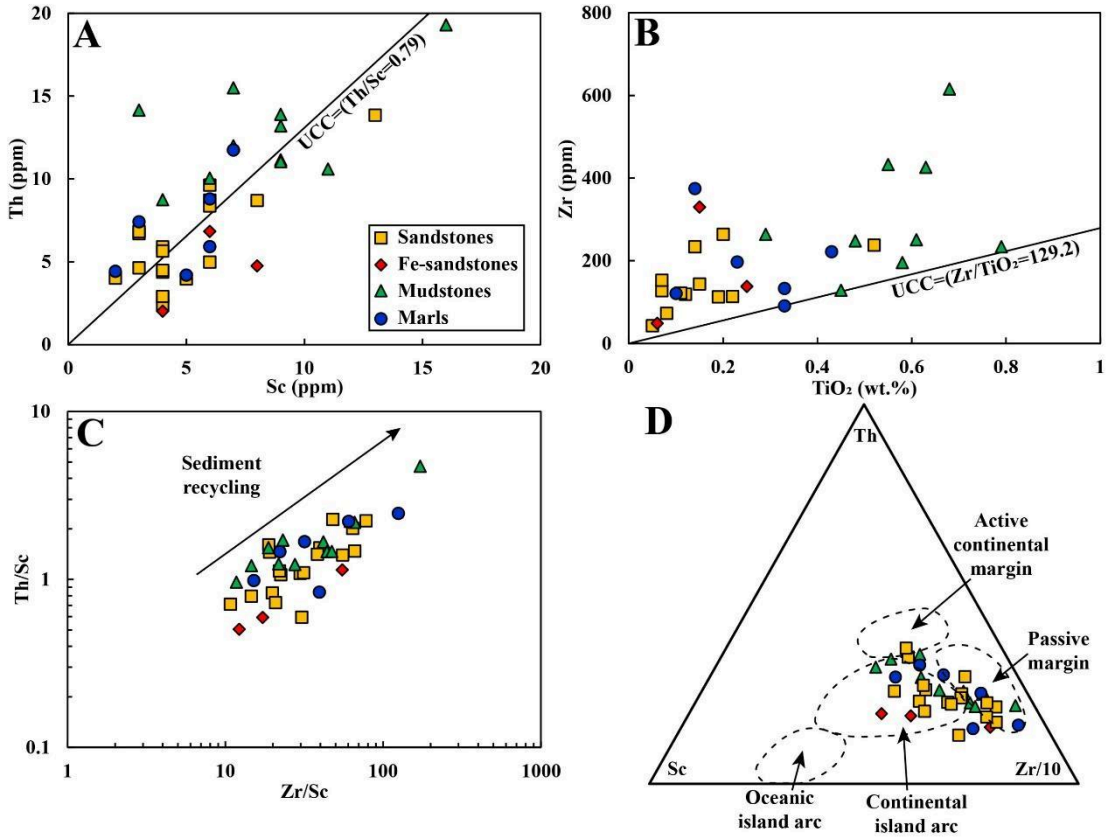

Figure 9: Diagrams for source rock composition discrimination, A) Th vs. Sc and B) Zr vs. TiO_2, lines are after UCC ratios (Mclennan, 2001); C) Th/Sc vs. Zr/Sc diagram for evaluation of sedimentary sorting and recycling/zircon addition (McLennan et al., 1993); D) Th-Zr/10-Sc diagram for tectonic setting discrimination (Bhatia & Crook, 1986).

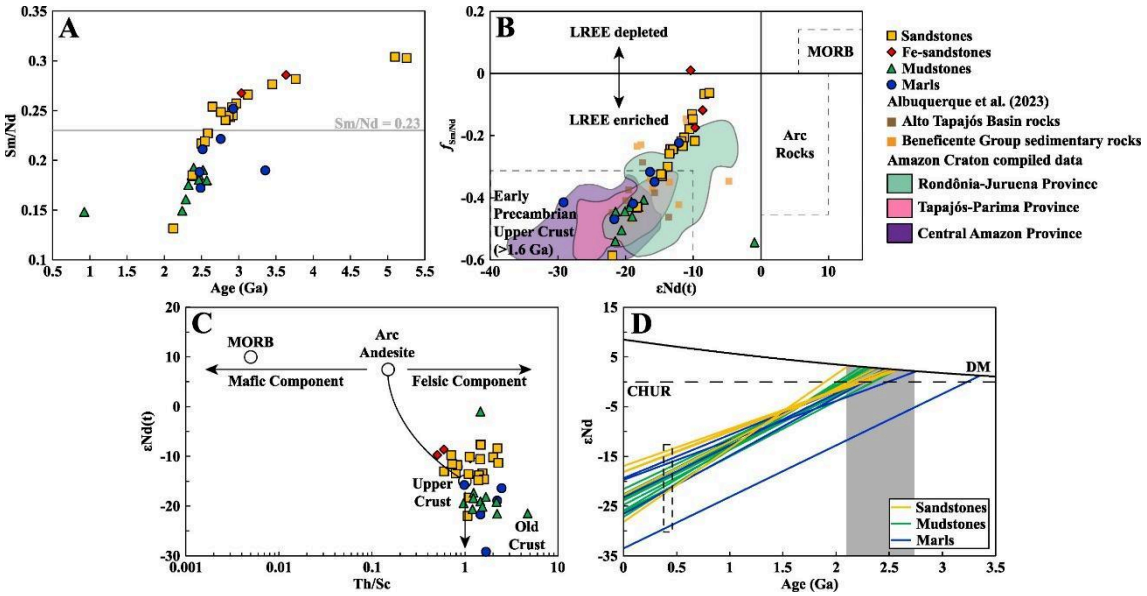

Figure 10: Diagrams for A – Sm/Nd ratio vs. T_{DM} model age; B – $f_{Sm/Nd}$ vs. εNd(t); C – εNd(t) vs. Th/Sc; and D – εNd vs. T_{DM} (only for mudstones and marls).

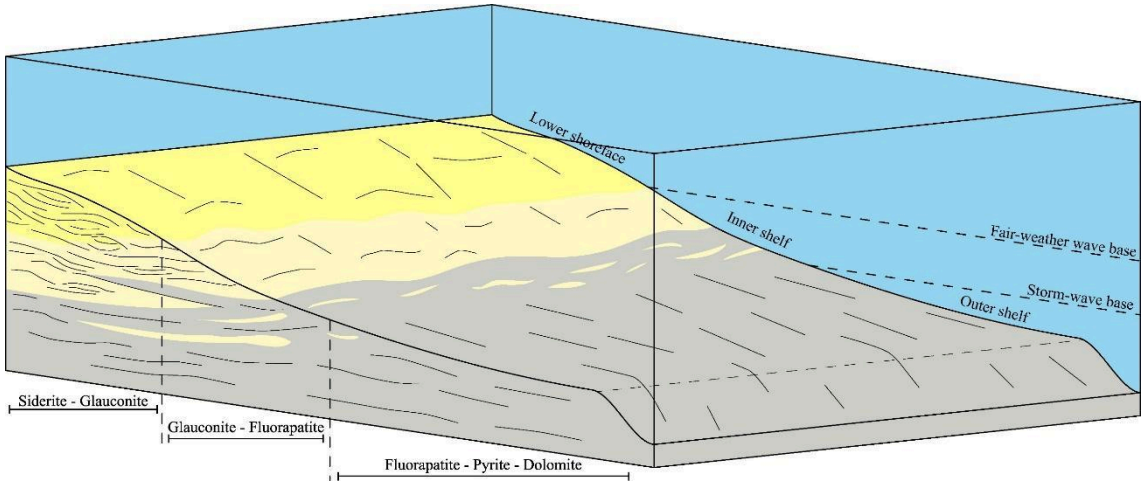

Figure 11: Schematic depositional model of the studied succession.

References

Albuquerque, M. F. dos S., Horbe, A. M. C., Simões, M. S., Aguiar Borges, C. C., & Dantas, E. L. (2023). Paleoproterozoic, Mesoproterozoic, and Paleozoic sedimentary successions of the Southwestern Amazonian craton: Geochemistry, provenance, and post-sedimentary events. *International Geology Review*, 1–30. https://doi.org/10.1080/00206814.2023.2266754

Almeida, M. E., Oliveira, A. C. da S., & Costa, U. A. P. (2016). *Geologia e recursos minerais da Folha Sumaúma—SB.20-Z-D, Estado do Amazonas, escala 1:250.000* (p. 250). CPRM.

Amorosi, A., Sammartino, I., & Tateo, F. (2007). Evolution patterns of glaucony maturity: A mineralogical and geochemical approach. *Deep-Sea Research Part II: Topical Studies in Oceanography*, *54*(11–13), 1364–1374. https://doi.org/10.1016/j.dsr2.2007.04.006

Bhatia, M. R., & Crook, K. A. W. (1986). Trace element characteristics of graywackes and tectonic setting discrimination of sedimentary basins. *Contributions to Mineralogy and Petrology*, *92*(2), 181–193. https://doi.org/10.1007/BF00375292

Bizinella, G. A., Santiago, A. F., Melo, A. F. F. de, Santos, A. dos, Borges, F. R., Godoy, H. K., Yamaguti, H. S., Oliveira, J. R. de, Carmona, J. R. M., D'Antona, R. de J. G., Oliveira, R. L., Andrade, A. F. de, Melo, C. F. de, Matos, E. B. de O., Barreto, E. L., Santana, E. A. N., Souza, F. J. C. de, Moreira, H. L., Costi, H. T., … Jorge João, X. da S. (1980). *Projeto Tapajós Sucunduri: Relatório final*. CPRM.

Blatt, H. (1985). Provenance studies and mudrocks. *Journal of Sedimentary Research*, *55*(1), 69–75. https://doi.org/10.1306/212F8611-2B24-11D7-8648000102C1865D

Bock, B., McLennan, S. M., & Hanson, G. N. (1994). Rare earth element redistribution and its effects on the neodymium isotope system in the austin Glen Member of the Normanskill Formation, New York, USA. *Geochimica et Cosmochimica Acta*, *58*(23), 5245–5253. https://doi.org/10.1016/0016-7037(94)90308-5

Bouvier, A., Vervoort, J. D., & Patchett, P. J. (2008). The Lu–Hf and Sm–Nd isotopic composition of CHUR: Constraints from unequilibrated chondrites and implications for the bulk composition of terrestrial planets. *Earth and Planetary Science Letters*, *273*(1–2), 48–57. https://doi.org/10.1016/j.epsl.2008.06.010

Chang, J., Li, Y., & Lu, H. (2022). The Morphological Characteristics of Authigenic Pyrite Formed in Marine Sediments. *Journal of Marine Science and Engineering*, *10*(10). https://doi.org/10.3390/jmse10101533

Chen, J., Algeo, T. J., Zhao, L., Chen, Z.-Q., Cao, L., Zhang, L., & Li, Y. (2015). Diagenetic uptake of rare earth elements by bioapatite, with an example from Lower Triassic conodonts of South China. *Earth-Science Reviews*, *149*, 181–202. https://doi.org/10.1016/j.earscirev.2015.01.013

Cullers, R. L. (1995). The controls on the major- and trace-element evolution of shales, siltstones and sandstones of Ordovician to tertiary age in the Wet Mountains region, Colorado, U.S.A. *Chemical Geology*, *123*(1–4), 107–131. https://doi.org/10.1016/0009-2541(95)00050-V

De Oliveira Carvalho, M., De Morisson Valeriano, C., Rodriguez Cabral Ramos, R., Heilbron, M., Aguiar Neto, C. C., Paravidini, G., & Do Eirado Silva, L. G. (2021). Tracing mantellic vs. crustal sources of clastic sediments in continental rifts using geochemical and Sm Nd and Sr isotope compositions: Insights from paleogene alluvial deposits of the Resende Basin, SE-Brazil. *Chemical Geology*, *586*, 120596. https://doi.org/10.1016/j.chemgeo.2021.120596

DePaolo, D. J. (1981). Neodymium isotopes in the Colorado Front Range and crust–mantle evolution in the Proterozoic. *Nature*, *291*(5812), 193–196. https://doi.org/10.1038/291193a0

Dickinson, W. R., Beard, L. S., Brakenridge, G. R., Erjavec, J. L., Ferguson, R. C., Inman, K. F., Knepp, R. A., Lindberg, F. A., & Ryberg, P. T. (1983). Provenance of North American Phanerozoic sandstones in relation to tectonic setting. *Geological Society of America Bulletin*, *94*(2), 222. https://doi.org/10.1130/0016-7606(1983)94<222:PONAPS>2.0.CO;2

Dickinson, W. R., & Suczek, C. A. (1979). *Plate Tectonics and Sandstone Compositions*.

Ehrenberg, S. N., & Nadeau, P. H. (2002). Postdepositional Sm/Nd Fractionation in Sandstones: Implications for Neodymium-Isotope Stratigraphy. *Journal of Sedimentary Research*, *72*(2), 304–315. https://doi.org/10.1306/060901720304

El Bamiki, R., Séranne, M., Parat, F., Aubineau, J., Chellaï, E. H., Marzoqi, M., & Bodinier, J. L. (2023). Post-phosphogenesis processes and the natural beneficiation of phosphates: Geochemical evidence from the Moroccan High Atlas phosphate-rich sediments. *Chemical Geology*, *631*. https://doi.org/10.1016/j.chemgeo.2023.121523

Föllmi, K. B. (1996). The phosphorus cycle, phosphogenesis and marine phosphate-rich deposits. *Earth-Science Reviews*, *40*(1–2), 55–124. https://doi.org/10.1016/0012-8252(95)00049-6

Gioia, S. M. C. L., & Pimentel, M. M. (2000). The Sm-Nd isotopic method in the geochronology laboratory of the University of Brasília. *Anais Da Academia Brasileira de Ciências*, *72*(2), 219–245. https://doi.org/10.1590/S0001-37652000000200009

Glenn, C. R., & Arthur, M. A. (1988). PETROLOGY AND MAJOR ELEMENT GEOCHEMISTRY OF PERU MARGIN PHOSPHORITES AND ASSOCIATED DIAGENETIC MINERALS: AUTHIGENESIS IN MODERN ORGANIC-RICH SEDIMENTS. *Marine Geology*, *80*, 231–267.

Haley, B. A., Klinkhammer, G. P., & McManus, J. (2004). Rare earth elements in pore waters of marine sediments. *Geochimica et Cosmochimica Acta*, *68*(6), 1265–1279. https://doi.org/10.1016/j.gca.2003.09.012

Jørgensen, B. B., D'Hondt, S. L., & Miller, D. J. (Orgs.). (2006). *Proceedings of the Ocean Drilling Program, 201 Scientific Results* (Vol. 201). Ocean Drilling Program. https://doi.org/10.2973/odp.proc.sr.201.2006

Kim, J., Kimura, Y., Puchala, B., Yamazaki, T., Becker, U., & Sun, W. (2023). Dissolution enables dolomite crystal growth near ambient conditions. *Science*, *382*(6673), 915–920. https://doi.org/10.1126/science.adi3690

López-Quirós, A., Sánchez-Navas, A., Nieto, F., & Escutia, C. (2020). New insights into the nature of glauconite. *American Mineralogist*, *105*(5), 674–686. https://doi.org/10.2138/am-2020-7341

Lumiste, K., Paiste, T., Paiste, P., Männik, P., Somelar, P., & Kirsimäe, K. (2023). REE + Y uptake in bioapatite revisited: Facies-controlled variability in coeval conodonts. *Chemical Geology*, *640*, 121761. https://doi.org/10.1016/j.chemgeo.2023.121761

McDaniel, D. K., Hemming, S. R., McLennan, S. M., & Hanson, G. N. (1994). Resetting of neodymium isotopes and redistribution of REEs during sedimentary processes: The Early Proterozoic Chelmsford Formation, Sudbury Basin, Ontario, Canada. *Geochimica et Cosmochimica Acta*, *58*(2), 931–941. https://doi.org/10.1016/0016-7037(94)90516-9

Mclennan, S. M. (2001). *Relationships between the trace element composition of sedimentary rocks and upper continental crust*.

McLennan, S. M. (2001). Relationships between the trace element composition of sedimentary rocks and upper continental crust. *Geochemistry, Geophysics, Geosystems*, *2*(4). https://doi.org/10.1029/2000GC000109

McLennan, S. M., Hemming, S., McDaniel, D. K., & Hanson, G. N. (1993). *Geochemical approaches to sedimentation, provenance, and tectonics* (p. 21–40). https://doi.org/10.1130/SPE284-p21

McLennan, S. M., Taylor, S. R., McCulloch, M. T., & Maynard, J. B. (1990). Geochemical and Nd□Sr isotopic composition of deep-sea turbidites: Crustal evolution and plate tectonic associations. *Geochimica et Cosmochimica Acta*, *54*(7), 2015–2050. https://doi.org/10.1016/0016-7037(90)90269-Q

Meinhold, G., Willbold, M., Karius, V., Jensen, S., Agić, H., Ebbestad, J. O. R., Palacios, T., Högström, A. E. S., Høyberget, M., & Taylor, W. L. (2022). Rare earth elements and neodymium and strontium isotopic constraints on provenance switch and post-depositional alteration of fossiliferous Ediacaran and lowermost Cambrian strata from Arctic Norway. *Precambrian Research*, *381*, 106845. https://doi.org/10.1016/j.precamres.2022.106845

Meister, P., Mckenzie, J. A., Vasconcelos, C., Bernasconi, S., Frank, M., Gutjahr, M., & Schrag, D. P. (2007). Dolomite formation in the dynamic deep biosphere: Results from the Peru Margin. *Sedimentology*, *54*(5), 1007–1032. https://doi.org/10.1111/j.1365-3091.2007.00870.x

Meloni, R. E., & Filho, P. B. (2017). *A sucessão vulcanossedimentar dos grupos Colíder e Beneficente no sudeste do Amazonas: Estilos eruptivos , tipos composicionais e ambientes de sedimentação*. *September*.

Milodowski, A. E., & Zalasiewicz, J. A. (1991). Redistribution of rare earth elements during diagenesis of turbidite/hemipelagite mudrock sequences of Llandovery age from central Wales. *Geological Society, London, Special Publications*, *57*(1), 101–124. https://doi.org/10.1144/GSL.SP.1991.057.01.10

Molina, J. M., Alfaro, P., Moretti, M., & Soria, J. M. (1998). Soft-sediment deformation structures induced by cyclic stress of storm waves in tempestites (Miocene, Guadalquivir Basin, Spain). *Terra Nova*, *10*(3), 145–150. https://doi.org/10.1046/j.1365-3121.1998.00183.x

Motta, M. B., Neves, M. P., Almeida, M. E., Reis, N. J., & D'Antona, R. G. de J. (2016). A pesquisa para fosfato na Bacia do Alto Tapajós, área Jatuarana, estado do Amazonas. Em *Projeto Fosfato Brasil: Parte II* (p. 1062–1188). CPRM. https://rigeo.sgb.gov.br/handle/doc/16142

Mücke, A. (2006). Chamosite, siderite and the environmental conditions of their formation in chamosite-type Phanerozoic ooidal ironstones. *Ore Geology Reviews*, *28*(2), 235–249. https://doi.org/10.1016/j.oregeorev.2005.03.004

Nesbitt, H. W., & Young, G. M. (1982). Early Proterozoic climates and plate motions inferred from major element chemistry of lutites. *Nature*, *299*(5885), 715–717. https://doi.org/10.1038/299715a0

Nesbitt, H. W., & Young, G. M. (1984). Prediction of some weathering trends of plutonic and volcanic rocks based on thermodynamic and kinetic considerations. *Geochimica et Cosmochimica Acta*, *48*(7), 1523–1534. https://doi.org/10.1016/0016-7037(84)90408-3

Nesbitt, H. W., & Young, G. M. (1989). Formation and Diagenesis of Weathering Profiles THE JOURNAL OF GEOLOGY FORMATION AND DIAGENESIS

OF WEATHERING PROFILES'. Em *Source: The Journal of Geology* (Vol. 97, Número 2, p. 129–147).

Nesbitt, H. W., & Young, G. M. (1996). Petrogenesis of sediments in the absence of chemical weathering: Effects of abrasion and sorting on bulk composition and mineralogy. Em *Sedimentology* (Vol. 43, p. 341–358).

Odin, G. S., & Matter, A. (1981). De glauconiarum origine. *Sedimentology*, *28*(5), 611–641. https://doi.org/10.1111/j.1365-3091.1981.tb01925.x

Paravidini, G., Reis, H. L. S., Heilbron, M., Carvalho, M. de O., Neto, C. C. A., & Valeriano, C. de M. (2021). Combined use of Sm–Nd isotopes and lithogeochemistry in the sedimentary provenance of the southern Ediacaran-Cambrian Bambuí foreland basin system, Brazil. *Journal of South American Earth Sciences*, *111*. https://doi.org/10.1016/j.jsames.2021.103429

Pourmand, A., Dauphas, N., & Ireland, T. J. (2012). A novel extraction chromatography and MC-ICP-MS technique for rapid analysis of REE, Sc and Y: Revising CI-chondrite and Post-Archean Australian Shale (PAAS) abundances. *Chemical Geology*, *291*, 38–54. https://doi.org/10.1016/j.chemgeo.2011.08.011

Pufahl, P. K., & Grimm, K. A. (2003). Coated phosphate grains: Proxy for physical, chemical, and ecological changes in seawater. Em *Geology* (Número 9, p. 801).

Pufahl, P. K., & Groat, L. A. (2017). Sedimentary and Igneous Phosphate Deposits: Formation and Exploration: An Invited Paper. *Economic Geology*, *112*(3), 483–516. https://doi.org/10.2113/econgeo.112.3.483

Reis, N. J. (2006). *Rochas carbonáticas da região de Apuí, Amazonas* (Informe de Recursos Minerais 12; Série Insumos Minerais para Agricultura, p. 69). CPRM - Serviço Geológico do Brasil. https://rigeo.sgb.gov.br/handle/doc/1739

Reis, N. J., Almeida, M. E., Riker, S. L., & Ferreira, A. L. (2006b). *Geologia e recursos minerais do estado do Amazonas*.

Reis, N. J., Oliveira, A. C. de, Oliveira, A. A. de, & Bahia, R. B. C. (2017). *Geologia e recursos minerais da folha Mutum SB.20-Z-B: Estado do Amazonas*. CPRM - Serviço Geológico do Brasil.

Reis, N., Riker, S., Pinheiro, S. da S., Nobre, J., Cruz, N. da C., & Costi, H. (2006a). Geologia dos rios Tapajós, Juruena (Bararati e São Tomé) e Teles Pires, porção sul do Cráton Amazônico, em área limítrofe dos estados do Amazonas, Pará e Mato Grosso. *Contribuições à Geologia da Amazônia*, *4*, 55–68.

Rizzotto, G. J., Alves, C. L., Rios, F. S., & Aparecida De Sant'Ana Barros, M. (2019). The Western Amazonia Igneous Belt. *Journal of South American Earth Sciences*, *96*, 102326. https://doi.org/10.1016/j.jsames.2019.102326

Roser, B. P., & Korsch, R. J. (1986). Determination of Tectonic Setting of Sandstone-Mudstone Suites Using SiO_2 Content and K_2O/Na_2O Ratio. *The Journal of Geology*, *94*(5), 635–650. https://doi.org/10.1086/629071

Roser, B. P., & Korsch, R. J. (1988). Provenance signatures of sandstone-mudstone suites determined using discriminant function analysis of major-element data. *Chemical Geology*, *67*(1–2), 119–139. https://doi.org/10.1016/0009-2541(88)90010-1

Santiago, A. F., Santos, J. O. S., & Maia, R. G. N. (1980). Estratigrafia Preliminar da Bacia Sedimentar do Alto Tapajós. *Congresso Brasileiro de Geologia, 31, Camboriú. Anais, SBG*, *2*, 786–797. Scopus.

Santos, J. O. S. (2003). Geotectônica dos Escudos das Guianas e Brasil-Central (parte 1/2). Em L. A. Bizzi, C. Schobbenhaus, R. M. Vidotti, & J. H. Gonçalves (Orgs.), *Geologia, Tectônica e Recursos Minerais do Brasil* (p. 169–195). CPRM.

Santos, J. O. S., Hartmann, L. A., Faria, M. S., Riker, S. R., Miguel, M., Almeida, M. E., & Mcnaughton, N. J. (2006). *a Compartimentação Do Cráton Amazonas Em Províncias: Avanços Ocorridos No Período 2000-2006*. 2–4.

Santos, J. O. S., Hartmann, L. A., Gaudette, H. E., Groves, D. I., Mcnaughton, N. J., & Fletcher, I. R. (2000). A New Understanding of the Provinces of the Amazon Craton Based on Integration of Field Mapping and U-Pb and Sm-Nd Geochronology. *Gondwana Research*, *3*(4), 453–488. https://doi.org/10.1016/S1342-937X(05)70755-3

Santos, J. O. S., Rizzotto, G. J., Potter, P. E., McNaughton, N. J., Matos, R. S., Hartmann, L. A., Chemale, F., & Quadros, M. E. S. (2008). Age and autochthonous evolution of the Sunsás Orogen in West Amazon Craton based on mapping and U–Pb geochronology. *Precambrian Research*, *165*(3–4), 120–152. https://doi.org/10.1016/j.precamres.2008.06.009

Scandolara, J. E., Correa, R. T., Fuck, R. A., Souza, V. S., Rodrigues, J. B., Ribeiro, P. S. E., Frasca, A. A. S., Saboia, A. M., & Lacerda Filho, J. V. (2017). Paleo-Mesoproterozoic arc-accretion along the southwestern margin of the Amazonian craton: The Juruena accretionary orogen and possible implications for Columbia supercontinent. *Journal of South American Earth Sciences*, *73*, 223–247. https://doi.org/10.1016/j.jsames.2016.12.005

Simões, M. S., Meloni, R. E., & Benevides Filho, P. R. R. (2021). Unidades litoestratigráficas. Em *Áreas de relevante interesse mineral (ARIM): Evolução crustal e metalogenia do sudeste do Amazonas, distrito aurífero Juma, estado do Amazonas* (p. 39–108). Serviço Geológico do Brasil - CPRM. https://rigeo.cprm.gov.br/handle/doc/22194

Simões, M. S., Meloni, R. E., & Santos, J. O. S. (2020). Stratigraphy, depositional environments and zircon U-Pb (LA-ICP-MS) ages of the Statherian volcano-sedimentary Beneficente Group: Implications for tectonics and gold mineralization in SW of the Amazon Craton. *Precambrian Research*, *345*(April), 105756. https://doi.org/10.1016/j.precamres.2020.105756

Toczeck, A., Schmitt, R. da S., da Silva Braga, M. A., & de Miranda, F. P. (2019). Tectonic evolution of the Paleozoic Alto Tapajós intracratonic basin—A case study of a fossil rift in the Amazon Craton. *Journal of South American Earth Sciences*, *94*, 102225. https://doi.org/10.1016/j.jsames.2019.102225

Tostevin, R., Shields, G. A., Tarbuck, G. M., He, T., Clarkson, M. O., & Wood, R. A. (2016). Effective use of cerium anomalies as a redox proxy in carbonate-dominated marine settings. *Chemical Geology*, *438*, 146–162. https://doi.org/10.1016/j.chemgeo.2016.06.027

Verma, S. P., & Armstrong-Altrin, J. S. (2013). New multi-dimensional diagrams for tectonic discrimination of siliciclastic sediments and their application to Precambrian basins. *Chemical Geology*, *355*, 117–133. https://doi.org/10.1016/j.chemgeo.2013.07.014

Vuillemin, A., Wirth, R., Kemnitz, H., Schleicher, A. M., Friese, A., Bauer, K. W., Simister, R., Nomosatryo, S., Ordoñez, L., Ariztegui, D., Henny, C., Crowe, S. A., Benning, L. G., Kallmeyer, J., Russell, J. M., Bijaksana, S., Vogel, H., & The Towuti Drilling Project Science Team. (2019). Formation of diagenetic siderite in modern ferruginous sediments. *Geology*, *47*(6), 540–544. https://doi.org/10.1130/G46100.1